ELSEVIER

Calcination engineering of urchin-like CoO_x-CN catalysts to enhance photothermocatalytic oxidation of toluene via photo-/thermo-coupling effect

Meng Zhang [a,b,c,e], Hui Gao [a,b,c,e], Jing Chen [c,d], Ehiaghe Agbovhimen Elimian [a,b,c,f], Hongpeng Jia [a,b,c,e,*]

[a] Xiamen Key Laboratory of Materials for Gaseous Pollutant Control, Institute of Urban Environment, Chinese Academy of Sciences, Xiamen 361021, China
[b] CAS Center for Excellence in Regional Atmospheric Environment, Institute of Urban Environment, Chinese Academy of Sciences, Xiamen, Fujian 361021, China
[c] Key Laboratory of Urban Pollutant Conversion, Institute of Urban Environment, Chinese Academy of Sciences, Xiamen, Fujian 361021, China
[d] Xiamen Institute of Rare-earth Materials, Haixi Institutes, Chinese Academy of Sciences, Xiamen, Fujian 361021, China
[e] University of Chinese Academy of Sciences, Beijing 100049, China
[f] Department of Chemical and Environmental Engineering, Faculty of Science and Engineering, University of Nottingham Ningbo China, Ningbo, Zhejiang 315100, China

A R T I C L E   I N F O

A B S T R A C T

Photothermocatalysis is usually the photoinduced thermal effect to drive the catalytic reaction assisted by high-oxidizing radials from photocatalysis. Herein, a carbon nitride-induced urchin-like catalyst Co_3O_4-CoO-CN (abbreviated as CoO_x-CN) with abundant peripheral branches is synthesized through the solvothermal reaction and calcination at different temperatures. An appropriate calcination temperature can remove partial CN structure and help to promote the light absorption, maintain the high specific surface area, and produce enough active oxygen species and active sites. CoO_x-CN-300 exhibits the good catalytic activity with toluene conversion of 83.8% and CO_2 yield of 79.6% under the full spectrum irradiation, where photocatalysis plays an important role in igniting catalytic reaction and light-to-thermal conversion provides high temperature to fulfil intermediates mineralization. Furthermore, light irradiation can enhance the light-driven thermocatalytic performance of CoO_x-CN-300 compared to conventional thermocatalytic activity by activating more lattice oxygen and inducing the formation of more oxygen vacancies to participate in the oxidation reaction.

1. Introduction

The rapid development of urbanization and industrialization has resulted in the continuous growth of volatile organic compounds (VOCs) emission, which can react with other active species in the atmosphere to form air pollutants such as ozone and secondary organic aerosols (SOAs) [1]. Extensive studies on VOCs decomposition have been conducted for the urgent environmental protection and human health needs. Among all kinds of VOCs treatment schemes, catalytic oxidation has been recognized as the most effective method due to its high performance and low operating temperature [2,3]. However, it is normally inevitable to consume electricity power to provide the reaction energy for VOCs degradation. Over the past several decades, solar energy has been utilized for the photocatalytic degradation of VOCs by stimulating the semiconductor to generate strong oxidizing species for the oxidation reaction [4]. Unfortunately, it's still confronted with the challenge of low activity. Also, a majority of energy in the sunlight has been lost in the form of heat, due to the rapid recombination of charge carriers and the fact that light with longer wavelength cannot be exploited by the semiconductor materials. To make more use of sunlight, photothermocatalytic oxidation has been proposed, which fully takes advantages of both high-energy UV–vis light and infrared light with thermal effect [5,6]. Therefore, robust photothermocatalysts have been designed to meet the needs of low energy consumption and high catalytic performance.

Transition metal oxides, such as cobalt oxide, manganese oxide, iron oxide, are popular for the catalytic oxidation of VOCs (e.g. formaldehyde, toluene, benzene), owing to the low cost and high catalytic

Table 1
Physical properties and element contents of catalysts.

Catalysts	S_{BET} (m²/g)	Pore volume (cm³/g)	Pore diameter (nm)	d (nm)	Molar ratio by XPS		Co content by XPS (wt%)	C content (wt %)	N content (wt %)	OSC (μmol/g)
					Co (III)/Co (II)	O_{ads}/ O_{latt}				
CN	35.0	0.24	3.9	–	–	–	–	34.5	61.2	–
CoO	17.8	0.06	3.7	–	–	–	–	–	–	–
CoO-CN	66.8	0.29	3.9	30.3	–	12	44.6	9.4	13.0	4.8
CoO$_x$-CN-300	45.0	0.21	3.1	12.6	0.9	0.9	61.9	5.7	8.9	12.0
CoO$_x$-CN-400	24.8	0.08	3.3	11.5	1.1	0.6	70.4	0.4	0.3	12.8
CoO$_x$-CN-500	10.2	0.04	3.0	20.7	1.2	0.5	69.8	0.3	0.3	8.0

d, average crystallite size according to the Scherrer equation.

activity of these catalysts [7,8]. Among them, cobalt-based catalysts have become a hot research topic ascribing to its abundant valence and oxygen species related to redox properties [9,10]. Encouragingly, the reported excellent activity of cobalt-based catalyst could even be comparable to that of noble metal catalyst [11]. The modulation of electronic structure by doping heteroatom has been confirmed as an effective way to improve the reactivity of catalysts, where the doped heteroatoms can alter the crystal lattice of metal oxides and be further propitious to expose more defects and produce more active oxygen species for enhancing the catalytic activity [12,13]. As we all know, g-C$_3$N$_4$ (CN) can bond with metal oxide to regulate its electronic structure, since N atoms provide lone pair electrons as ligands to connect with transition metals [14,15]. Furthermore, CN also owns the better response capability of light. Our recent study has demonstrated that the proper addition of CoO in Pt-Co$_x$/CN exhibited the robust catalytic activity via improving the physical and chemical properties, such as the light absorption, the proportion and mobility of active oxygen species and the adsorption for toluene [16]. Unfortunately, low content of CoO combined with CN (CoO/CN) still need to be modified the electronic structure with noble metal Pt for promoting the catalytic activity of the catalyst. High temperature and high pressure can dramatically strengthen the connection of metal oxide and C/N, even form heteroatoms doping in the crystal phase of metal oxide, which is more advantageous to catalytic reaction by improving the physicochemical properties of metal oxide [17,18–20].

Herein, we synthesized a CoO-CN composite under solvothermal conditions, which was then thermally treated to obtain CoO$_x$-CN-T compounds at different temperatures. The samples were tested for composition and content, specific surface area, light absorption, the content of surface oxygen species and oxygen vacancies to illustrate the intrinsic structure properties. Furthermore, the photothermocatalytic degradation of toluene over the samples was conducted and explained related to the intrinsic structure. Photocatalytic and thermocatalytic tests and catalytic activities under different wavelengths of light were carried out, to distinguish their respective roles in photothermocatalytic reactions. Chemisorption experiments and EPR were performed under irradiation and in dark to further explore the influence of photo.

2. Experimental section

2.1. Chemicals

Melamine is C.R. grade and other chemicals are A.R. grade. All the reagents during catalyst preparation were directly used without further purification. Melamine, absolute ethanol (CH$_3$CH$_2$OH), n-octanol (C$_8$H$_{18}$O), cobalt (II) acetate tetrahydrate (Co(CH$_3$COO)$_2$.4H$_2$O) were purchased from Sinopharm Chemical Reagent Co., Ltd.

2.2. Catalyst preparation

CN powder was obtained by calcining melamine in the tube furnace under air atmosphere at 550 °C for 4 h. Prior to solvothermal reaction, 1 g of CN was added to 60 mL of solution consisting of absolute ethanol and n-octanol (ethanol: n-octanol = 4: 1), and then stirred for 1 h. Then 7.75 g of Co(CH$_3$COO)$_2$.4 H$_2$O was added and kept stirring for another 2 h. The resulted mixture was transferred into a 100 mL Teflon-lined stainless-steel autoclave and put it in an oven to be heated at 220 °C for 4 h. After cooling to room temperature, the slurry was filtered and washed with absolute ethanol for several times. Finally, the collected solids of CoO-CN were dried in an oven at 80 °C, which is used as an uncalcined reference sample. ~~and then~~ Then CoO-CN were further calcined in the tube furnace at different temperatures (300, 400 and 500 °C) under air atmosphere and the obtained samples were named as CoO$_x$-CN-T according to the calcination temperatures. As the reference sample, pure CoO were prepared under the same solvothermal conditions but without CN addition.

2.3. Catalyst characterization and catalytic tests

The catalysts were characterized by various techniques such as thermal gravimetric analyzer (TGA), X-ray diffraction (XRD), Fourier transform infrared (FTIR), Raman spectroscopy, high-resolution transmission electron microscopy (HR-TEM), high-angle annular dark-field scanning transmission electron microscopy (HAADF-STEM), nitrogen adsorption-desorption measurements, diffuse reflectance spectra (DRS), X-ray photoelectron spectroscopy (XPS), O$_2$-temperature-programmed desorption (O$_2$-TPD) in dark and under illumination, H$_2$-temperature-programmed reduction (H$_2$-TPR) in dark and under illumination, oxygen storage capacity (OSC), toluene-temperature-programmed desorption (toluene-TPD) in dark and under illumination, electron paramagnetic resonance (EPR), photocurrent test, in situ diffuse reflectance infrared Fourier transform (DRIFT) spectroscopy. The catalytic activities of the samples were evaluated by studying toluene oxidation in a cylindrical stainless-steel reactor. All the details of characterization and catalytic tests are recorded in the Supporting information.

3. Results and discussion

3.1. Physical structure and surface properties

Thermal treatment to initial CoO-CN at different temperatures in air causes different amount of C and N residual in the samples, which thereby influences physicochemical properties of the catalysts. As TGA results depicted in Fig. S1, during the process of annealing in air atmosphere, the weight loss of CoO-CN is more obvious above 250 °C and reaches to the maximum value of around 26.6% at 480 °C (the weight loss is 23.0% between 250 and 480 °C), which is much closer to the CN
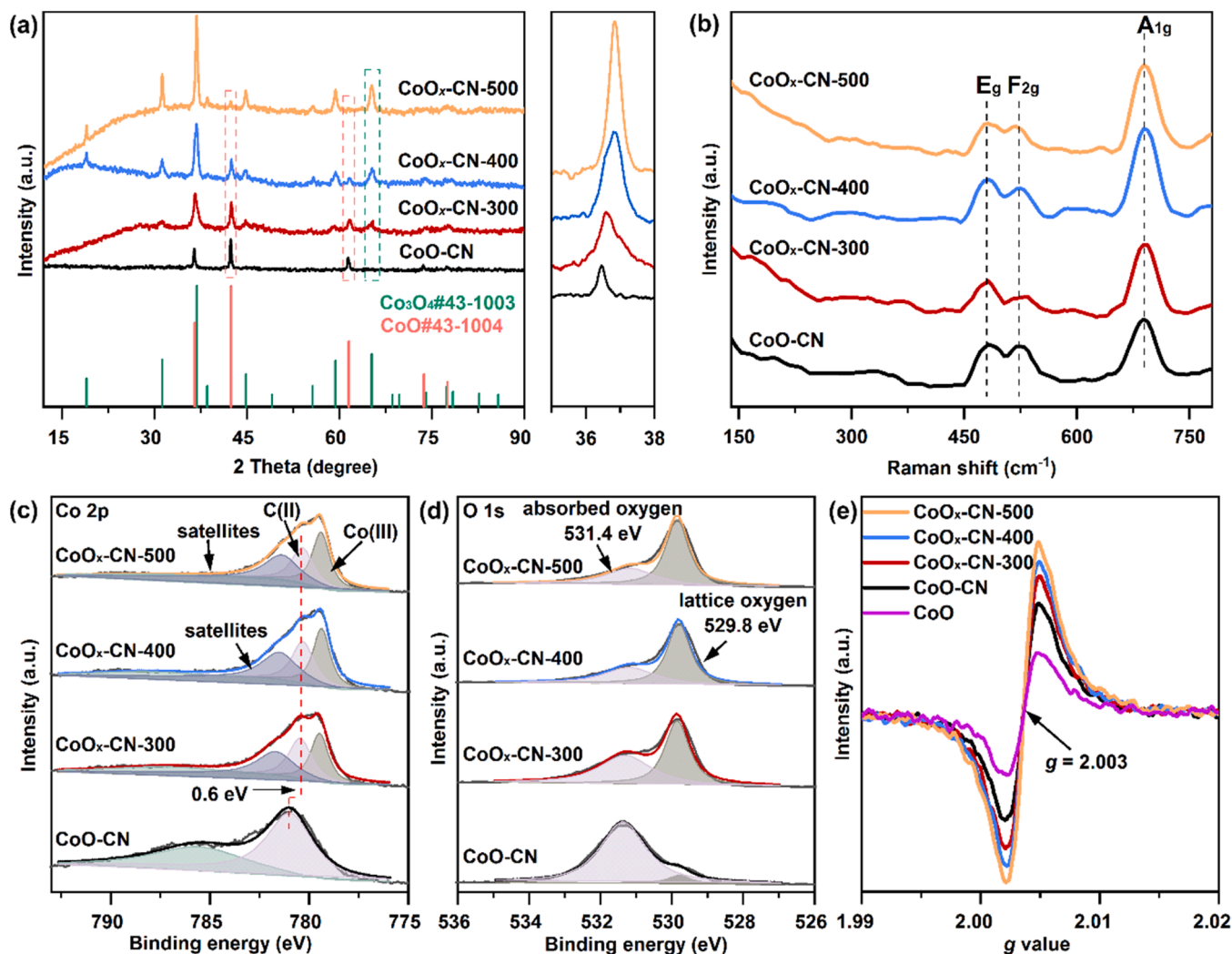
Fig. 1. (a) XRD patterns, (b) Raman spectra, (c) Co 2p and (d) O 1 s XPS spectra, (e) EPR profiles at room temperature of the CoO-CN, CoO$_x$-CN-300, CoO$_x$-CN-400 and CoO$_x$-CN-500.

actual content of 22.4% in CoO-CN (the carbon content is 9.4% and the nitrogen content is 13.0%, as displayed in Table 1). Almost all CN in CoO-CN can be removed at 480 °C. With annealing above 500 °C, the weight loss is reduced to ca. 25.4%, which is due to the oxidation of some Co(II) to form Co(III) [21]. It is also confirmed by investigating FTIR spectra of all samples (Fig. S2). The low-temperature treated sample such as CoO$_x$-CN-300 still can be well observed the characteristic absorption peaks of CN accompanying with the appearance of obvious Co$_3$O$_4$ characteristic peaks at 574 and 665 cm^{-1}, which states the existence of CN and the transformation of CoO to Co$_3$O$_4$ [22–24], With treatment temperature up to 400 and 500 °C, CoO$_x$-CN-400 and CoO$_x$-CN-500 display the total disappearance of CN peaks and the prominent Co$_3$O$_4$ peaks. Combined with the elemental analysis of samples (Table 1), CoO-CN and CoO$_x$-CN-300 exhibit the obvious existence of C and N, however, CoO$_x$-CN-400 and CoO$_x$-CN-500 only give the very-low C and N contents. It manifests that high-temperature removes the main CN by destroying its structure and simultaneously remains a small amount of C and N in the form of elemental doping in the samples.

XRD pattern of CoO-CN exhibits the typical characteristic peaks of CoO indexed as the standard card (JCPDS No. 43–1004), as shown in Fig. 1a. No obvious evidence for CN diffraction peaks appears, which indicates the loss of the crystalline structure of CN under high temperature, high pressure and high concentration of Co ions. CoO$_x$-CN-300

still retains the main crystal phase of CoO but also shows the characteristic peaks of Co$_3$O$_4$ (JCPDS No. 43–1003). With the increase of calcination temperature from 300 °C to 500 °C, the intensity of Co$_3$O$_4$ peaks is gradually enhanced along with the disappearance of CoO peaks. The average grain size (Table 1) of CoO-CN is obtained by calculating (200) crystalline plane by Scherrer equation, which is 30.3 nm. The average grain size of CoO-CN-T is obtained by calculating (311) crystalline plane, which are 12.6, 11.5 and 20.7 nm, respectively. The calcination of CoO-CN reduces the particle size and exposes more active sites, which is conducive to the catalytic reaction. The increasing calcination temperature promote the particles agglomeration, thus making the mean grain size larger. The evolution of catalyst structure was further confirmed by Raman spectroscopy results (Fig. 1b). Cobalt oxides present three strong bands at 420, 530 and 687 cm^{-1} corresponding to E$_g$, F$_{2g}$, and A1g, respectively [25,26]. The most intense peak of A$_{1g}$ at 687 cm^{-1} is distinguished as the vibration of CoO$_6$ sites in cobalt oxides, which is intensified with the increasing of Co(III) derived from Co$_3$O$_4$ [27].

XPS results of Co 2p and O 1 s spectra are illustrated in Figs. 1c and 1d. For CoO-CN, the apparent peaks at 781.0 and 785.5 eV are assigned to Co(II) species and its shakeup satellite peak [28]. Calcination treatment transformed partial CoO of CoO-CN into Co$_3$O$_4$, therefore, Co 2p3/2 XPS spectra emerged at 776 – 792.7 eV of calcined samples can be deconvoluted into four peaks, among which the peaks appeared at
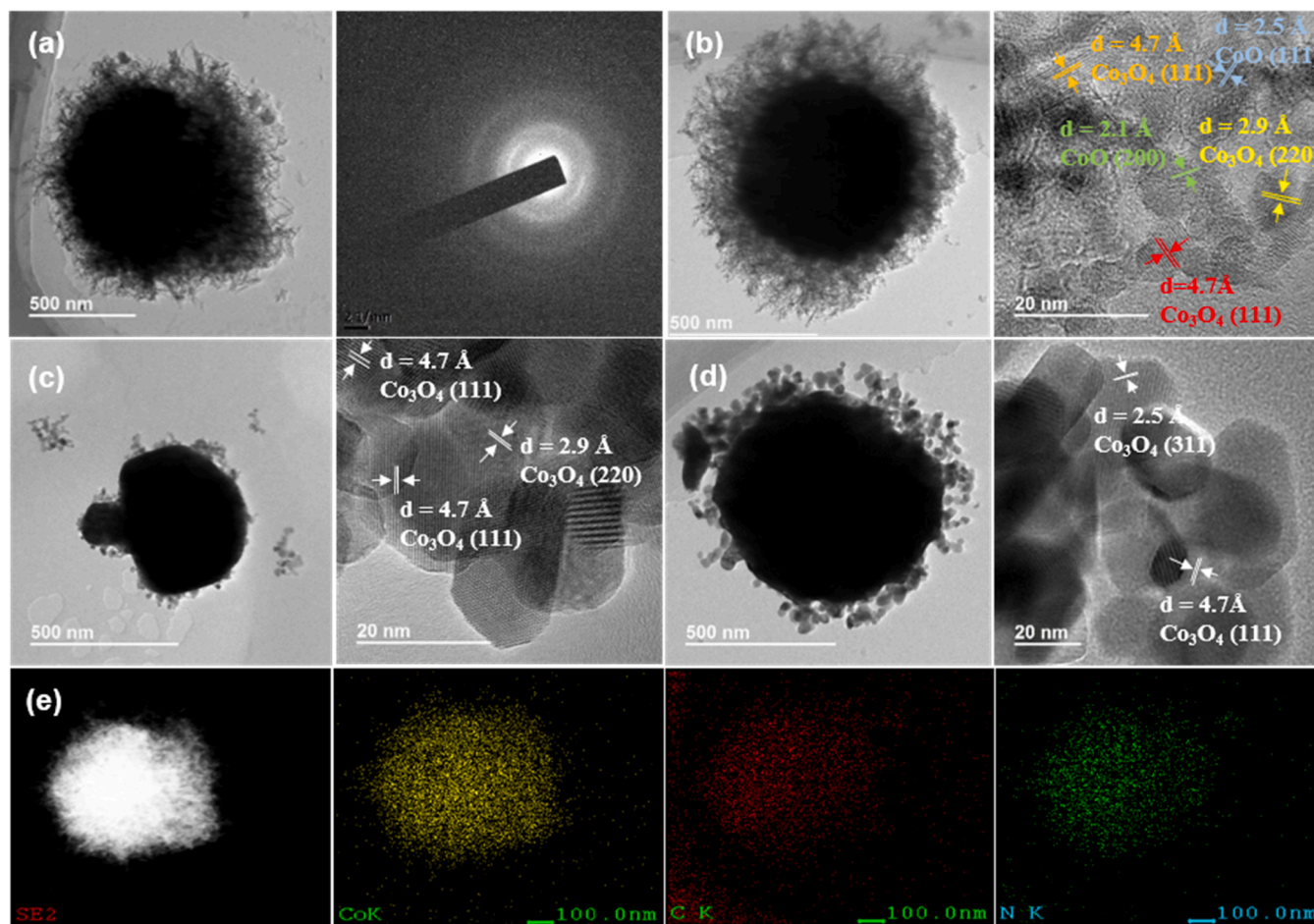
Fig. 2. HR-TEM images of CoO-CN (a), CoO$_x$-CN-300 (b), CoO$_x$-CN-400 (c), CoO$_x$-CN-500 (d), and HAADF-STEM image and element mapping of CoO-CN (e).

779.5 eV and 780.5 eV indicate the copresence of Co(III) and Co(II) species [29,30]. Besides, the band located at 788.2 eV corresponds to the shakeup satellite of Co(III). The peak ascribed to Co(II) of calcined samples (CoO$_x$-CN-300, CoO$_x$-CN-400 and CoO$_x$-CN-500) showed a negative shift compared to CoO-CN, demonstrating the augment of outer electron density of cobalt atom. This is due to the removal of high-electronegativity C/N and the formation of significant lattice distortion [31,32]. For the electron binding energy of some transition metal elements such as cobalt, the presence of the transition of valence electrons from occupied orbits to higher unoccupied orbits, commonly known as the shakeup satellites, can be observed near 785 eV [33,34]. This process is frequently used as an auxiliary means to distinguish the chemical state of elements between Co(II) oxides and Co(III) oxides, there is no multiple electron excitation for Co(III) [30]. Subsequently, the atomic ratio of Co(III) and Co(II) was calculated, as exhibited in Table 1. With the elevating of calcination temperature, the ratio of Co(III)/Co(II) increases. At the same time, carbon content and nitrogen content present a descending trend. Co(III) is generally considered to be the active site for VOCs catalytic oxidation and the samples calcined at higher temperatures possess higher Co(III) concentration [35,36]. The O 1s spectra are mainly divided into two peaks, corresponding to lattice oxygen (529.8 eV) and adsorption oxygen (531.4 eV) [37]. The proportion of oxygen species adsorbed on the surface of catalysts decreases gradually with the increase of calcination temperature (Table 1), assigned to the reduction of CN content and the specific surface area.

As shown in Fig. 1e, the intensity of EPR signal at 2.003 corresponding to the oxygen vacancies follows the order: CoO < CoO-CN < CoO$_x$-CN-300 < CoO$_x$-CN-400 < CoO$_x$-CN-500, which indicate that the CN-doped CoO-CN composite possess more oxygen defects than CoO

due to the formation of p-n heterojunction [28],[38] Generally, heteroatom doping can cause the lattice distortion of metal oxide to generate oxygen vacancies [12]. Thermal treatment at different temperatures remove partial CN structure, leaving more oxygen vacancies. The number of oxygen vacancies increases with the rising of calcination temperature, exerted by the loss of interaction between CN and metal oxides. Therefore, the destruction of CN results in the positive formation of oxygen vacancies.

HRTEM image of CoO-CN displays the urchin-like morphology with abundant peripheral branches (Fig. 2a), where the dispersive diffraction rings indicate the poor crystallinity of sample (as observed in XRD pattern). The urchin-like structure makes CoO-CN possess a larger specific surface area of 66.8 m^2/g compared to pure CoO (17.8 m^2/g) and CN (35.0 m^2/g) (Fig. S3 and Table 1). HAADF-STEM image and element mapping of CoO-CN (Fig. 2e) display the uniform overlapping distribution of Co, C and N elements in the same district, indicating the tight combination of CoO and CN. In the high-temperature liquid medium, the long-range ordered arrangement of CN layers is disturbed by the evolution of fluctuations of liquid, resulting in the formation of nanobelt structure [39]. Combined with CoO$_x$ particles, it shows an urchin-like structure. Further thermal treatment at 300 °C remains the peripheral branches of urchin-like structure and forms the identified lattice pattern and lattice space of CoO and Co$_3$O$_4$, as observed in HRTEM images of CoO$_x$-CN-300 (Fig. 2b and S4). When the calcination temperature was increased to above 300 °C, the surrounding peripheral branches shrank into nanoparticles in CoO$_x$-CN-400 and CoO$_x$-CN-500 (Fig. 2(b−d)). High-temperature treatment induced structure change of catalyst leads to the obvious decrease of specific surface areas from 45.0 m^2/g to 10.2 m^2/g and pore volumes from 0.21 cm^3/g to 0.04 cm^3/g,
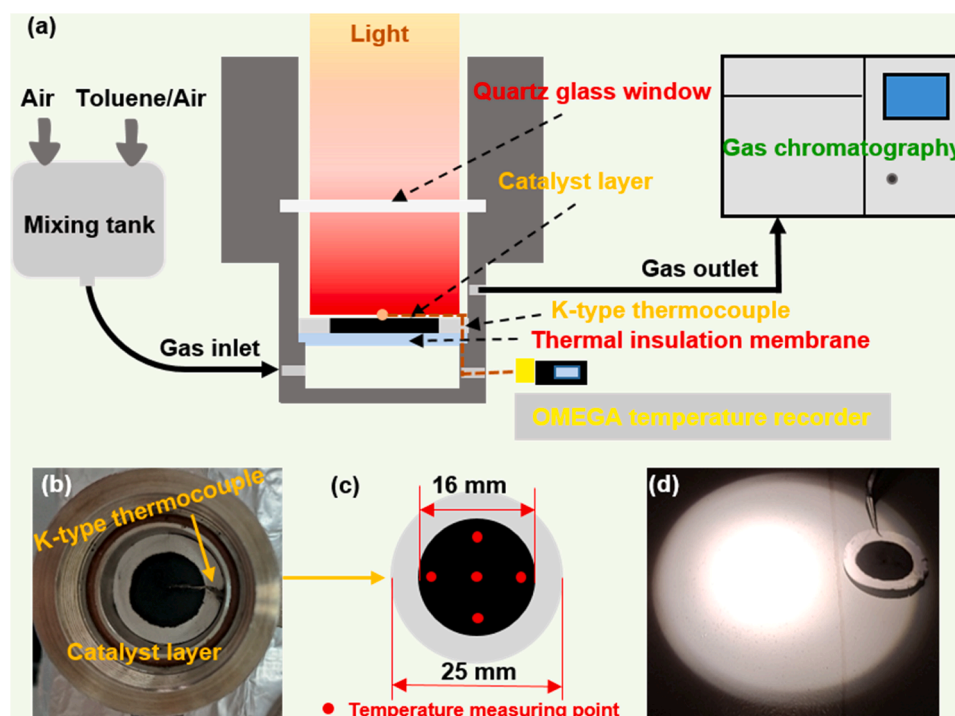
Fig. 3. (a)The schematic diagram for illustration of photothermocatalytic setup and (b) the picture of loading catalyst in the reactor, (c) schematic diagram of the catalyst layer (The same temperature observed at the five temperature measuring points), (d) the picture of concentrated light emitted from Xenon lamp.
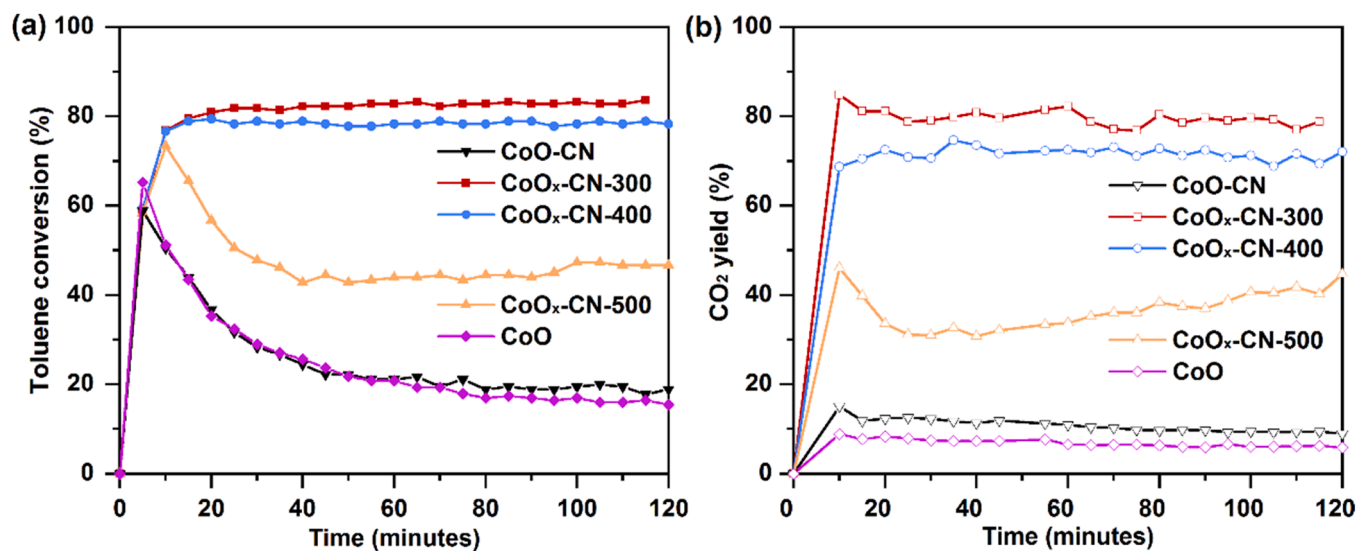

Fig. 4. (a) Toluene conversion and (b) CO_2 yield over the catalysts under full spectrum irradiation with light intensity of 451 mW/cm^2.

respectively. However, pure CoO only shows simple polyhedron morphology without peripheral branch and low specific surface area of 17.8 m^2/g (Fig. S5 and Table 1). These results imply that CN plays an important role in the formation of the urchin-like structure, where the introduction of CN during the solvothermal synthesis process is conducive to expand the surface area of metal oxides[40].

3.2. Photothermocatalytic performance in toluene oxidation

The reaction setup is shown in Fig. 3 to display the photothermal reaction process. As illustrated in Fig. 3a, the equilibrium of toluene (air) with a concentration of 200 ppm around was established in a mixing tank by blowing out toluene vapor through air. The catalytic activities of

the samples for toluene oxidation were evaluated in a cylindrical stainless steel reactor. At the top of the reactor is a quartz window from which light is emitted. The temperature of catalyst layer was measured by a K-type thermocouple and recorded by Omega temperature recorder. Before the test, the catalyst is evenly distributed in ethanol solvent and coated on the glass fiber membrane with a diameter of 25 mm through a suction filtration device with an inner diameter of 16 mm (Figs. 3b and 3c). Therefore, 30 mg of catalyst is stacked in a range of 16 mm in diameter, which is just in the middle of the light. Under light irradiation, 5 temperature measuring points have been selected to detect the temperature. It is found that the temperature at these points is the same, which is 218 °C over CoO-CN-300 under the light intensity of 451 mW/cm^2. Actually, the temperature on the catalyst

Table 2

Catalytic performance of catalysts under the irradiation of different light sources.

Catalysts	Light sources	Light intensity (mW/cm^2)	Temperature (°C)	Toluene conversion (%)	CO$_2$ yield (%)
CoO-CN	UV–vis-IR	451	205	19.4	9.4
	UV–vis	505	215	10.5	7.5
	IR (>800 nm)	321	203	15.6	8.1
CoO$_x$-CN-300	UV–vis-IR	451	218	83.8	77.7
	UV–vis	505	218	73.6	62.3
	IR (>800 nm)	321	218	72.1	63.4
CoO$_x$-CN-400	UV–vis-IR	451	228	78.9	71.7
	UV–vis	505	226	28.2	17.6
	IR (>800 nm)	321	226	74.7	63.9
CoO$_x$-CN-500	UV–vis-IR	451	242	49.4	43.6
	UV–vis	505	228	17.3	9.5
	IR (>800 nm)	321	233	34.0	18.6

surface is very uniform and stable in the concentrated light range (Fig. 3d). Also, the bed layer thickness is less than 1 mm, hence the temperature from top to bottom is also very uniform. Simultaneously, the temperature of the catalyst layer is recorded through a temperature record, and a temperature point is recorded every two seconds.

Photothermocatalytic tests for toluene oxidation over these catalysts

were implemented (Fig. 4). Under full spectrum irradiation with the light intensity of 451 mW/cm^2, the toluene conversion and CO$_2$ yield of the catalysts obey the order as follows: CoO < CoO-CN < CoO$_x$-CN-500 < CoO$_x$-CN-400 < CoO$_x$-CN-300. CoO-CN displays the slightly better catalytic performance than CoO due to the formation of heterojunction between CN and CoO. Also, heteroatom doping facilitates the formation of oxygen vacancies by distorting the crystal structure, which usually play an important role in catalytic oxidation by adsorbing and activating reactant molecules [19]. The calcination treatment further promotes the catalytic activity on CoO$_x$-CN-300 with toluene conversion of 83.8% and CO$_2$ yield of 79.6%, respectively. As the calcination temperature was further increased to 400 °C and 500 °C, the catalytic activities were reduced, where CoO$_x$-CN-400 and CoO$_x$-CN-500 presents toluene conversion of 77.8% and 46.7%, respectively, the corresponding CO$_2$ mineralization is 71.6% and 41.7%. Associated with the above structural properties of catalysts, the synergetic effect of the large specific surface area, pore volume, moderate oxygen vacancy content and high Co(III) ratio may lead to the more superior toluene degradation performance of CoO$_x$-CN-300 than other samples. To identify the contribution of dominant spectral range in the whole region, the catalytic tests under different light sources were carried out and the reaction rate of the catalysts were summarized in Table 2. Firstly, light in different band ranges was used as light source to make CoO$_x$-CN-300 catalyst layer achieve the temperature of 218 °C. The order of light intensity follows: UV–vis (505 mW/cm^2) > UV–vis-IR (451 mW/cm^2) > IR (321 mW/cm^2), since IR part has strong thermal effect. Under
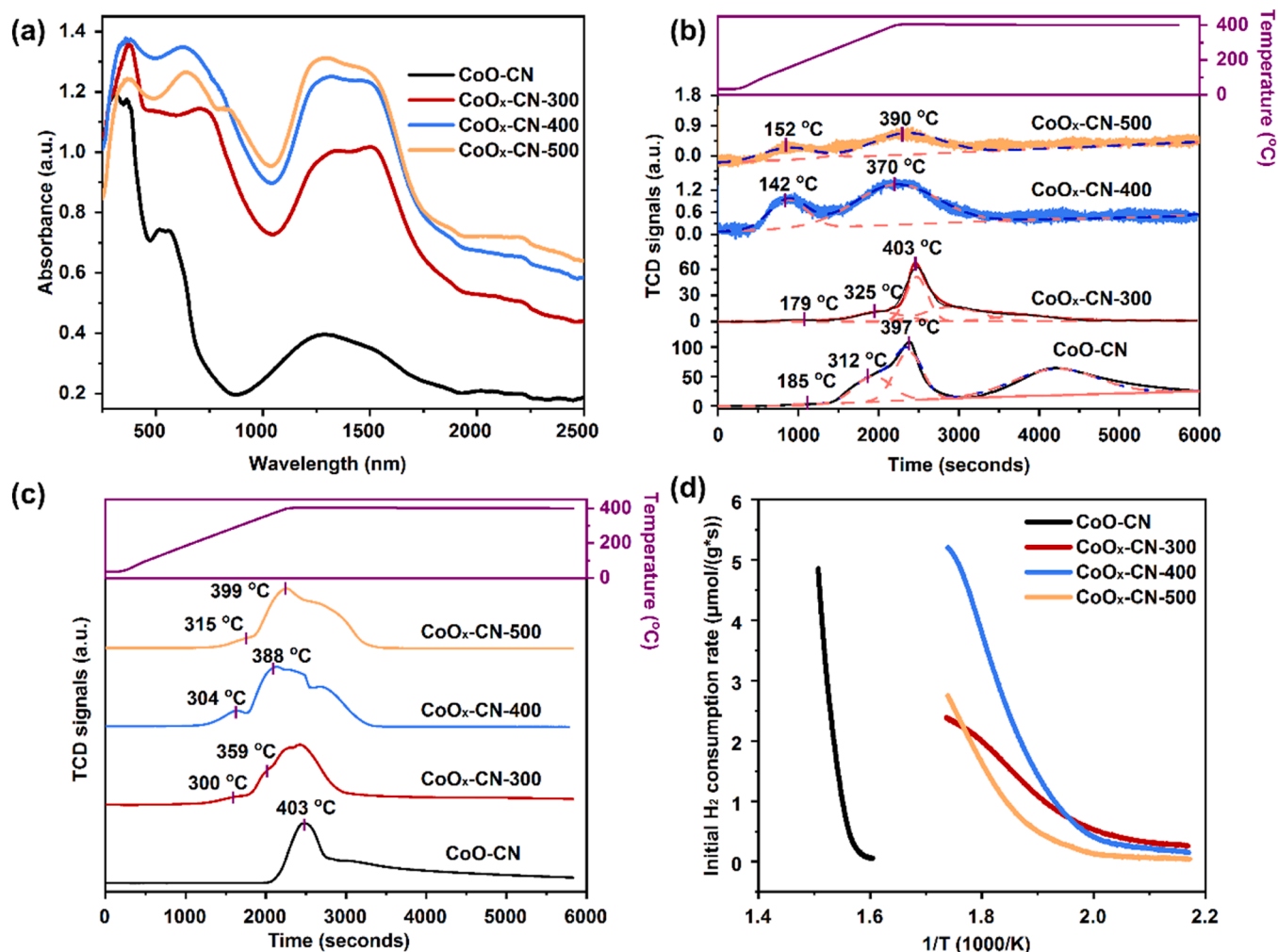

Fig. 5. (a) UV–vis−IR DRS spectra of the samples, (b) O$_2$-TPD, (c) H$_2$-TPR profiles and (d) initial H$_2$ consumption rate ($r_{initial}$) at low temperature over samples.

Table 3
Quantitative results of O_2-TPD and H_2-TPR.

Samples	Amount of desorbed O_2 in O_2-TPD (μmol/g)				Amount of H_2 in H_2-TPR (μmol/g, 50–400 °C)
	Total amount (50–400 °C)	O_{Ads}	O_{Suf}	O_{Bulk}	
CoO-CN	4270	13	895	3362	13,235
CoO$_x$-CN-300	2699	77	357	2265	14,655
CoO$_x$-CN-400	90	22	67	0	19,596
CoO$_x$-CN-500	52	15	37	0	19,230

UV–vis light intensity of 505 mW/cm^2, temperature over CoO$_x$-CN-300 (218 °C) and CoO$_x$-CN-400 (226 °C) is almost equal to that under full spectrum irradiation (218 °C for CoO$_x$-CN-300 and 228 °C for CoO$_x$-CN-400). However, the variation of temperature over CoO/CN and CoO$_x$-CN-500 presents opposite tendency. The temperature of CoO-CN is higher and CoO$_x$-CN-500 is lower under UV–vis irradiation than that under the full spectrum irradiation. The catalytic performance over all samples under UV–vis irradiation drops in contrast to that under the full spectrum and the activity order remains unchanged. When the temperature of CoO$_x$-CN-300 reaches 218 °C under IR irradiation (> 800 nm), the intensity of IR light presents 321 mW/cm^2. Under the same IR light intensity, the temperature over all samples is also approximately equal to that under the full spectrum but the catalytic activities decrease. Therefore, different wavelength ranges of light have a synergistic effect. Generally, high-energy UV–vis light can stimulate the semiconductor catalysts to produce holes and electrons that are in combination with oxygen and water to obtain highly-oxidized active oxygen species, finally resulting in the effective oxidation of VOCs via traditional photocatalytic process. Simultaneously, the photon energy absorbed by the semiconductor rapidly dissipates in the form of heat through charge carrier recombination. Localized thermal energy derived from charge carrier recombination and IR thermal effect will transfer to the active site and provide energy for the reaction, which is usually the most fundamental factor in the catalytic oxidation reaction [3]. Light irradiation may promote the lattice oxygen activation on the surface of catalysts by enhancing the low-temperature metal reducibility and mobility ability of lattice oxygen, thus improving the catalytic activity [16,41]. The combined effect of photo energy and thermal energy give rise to the difference of catalytic activity in the whole spectrum.

3.3. Origin of photothermocatalytic activity and photoactivation effects

The UV−vis−IR diffuse reflectance spectra (DRS) were applied to evaluate the light absorption capacity of catalysts (Fig. 5a). The absorption peak at 450 nm is attributed to the Co(II) spin–orbit bands [42]. After the calcination treatment of CoO-CN at different temperatures, the light absorption of the acquired catalysts over the entire spectral range is apparently enhanced. CoO$_x$-CN-400 and CoO$_x$-CN-500 display the broader and attenuated band at around 450 nm, which indicates the lessened amount of Co(II) in samples [6]. It is obvious to observe a new absorption peak at 700 nm for all thermally-treated samples, ascribing to the metal–metal charge transition of Co(III)−Co(II) (MMCT) and the absorption of low-spin Co(III) in octahedral sites [43]. Analogously, the wide band within the range of 1030–1830 nm is from the MMCT and the absorption of high-spin Co(II) in tetrahedral sites. The strong light absorption enables the catalyst to provide enough energy to raise the temperature. Under the same irradiation, all catalysts can absorb photon energy to soar the temperature to more than 200 °C rapidly (Fig. S6). Then the temperature reached equilibrium due to energy absorption and consumption, which were 205, 218, 228 and 242 °C over CoO-CN, CoO$_x$-CN-300, CoO$_x$-CN-400, CoO$_x$-CN-500, respectively.

The catalytic reactions of toluene oxidation usually occur at less than 300 °C, thus chemisorption experiments were conducted up to 400 °C and maintained for one hour, for the main attention of the oxygen desorption behavior and metal reducibility at low temperature. O_2-TPD profiles of CoO-CN and CoO$_x$-CN-T (Fig. 5b) display that the content of surface oxygen species on the catalyst is gradually reduced with increasing of calcination temperature. Generally, various surface oxygen species can be reflected by the desorption temperature owing to different binding ability on the surface of catalyst and obey the following sequence: physically adsorbed oxygen→ chemical adsorbed oxygen→ surface lattice oxygen→ bulk lattice oxygen [26]. O_2-TPD patterns of the samples have been fitted to identify the temperature and quantity of different desorbed oxygen species, as shown in Fig. 5b and Table 3. Considering that catalytic oxidation is usually in accordance with Mars-van Krevelen (MvK) mechanism over reducible transition-metal oxides, the mobility and amount of lattice oxygen (O_{latt}) of catalyst are commonly concerned. Both CoO-CN (312, 397 °C) and CoO$_x$-CN-300 (325, 403 °C) show two distinguishable peaks in the desorption temperature region of O_{latt}, but CoO$_x$-CN-400 and CoO$_x$-CN-500 only exhibit the broad peak centered at 370 and 390 °C, respectively. Although all samples have the similar desorption temperature region of O_{latt}, the desorbed O_{latt} amounts of CoO-CN and CoO$_x$-CN-300 are much more than that of CoO$_x$-CN-400 and CoO$_x$-CN-500, which can supply abundant active O_{latt} in the catalytic process of toluene oxidation. H_2-TPR profiles (Fig. 5c) reveal that CoO$_x$-CN-T samples possess the lower-temperature reducibility compared to CoO-CN. CoO$_x$-CN-300 gives the signal at 300 °C assigned to the reduction of Co(III) to Co(II), which is lower than CoO$_x$-CN-400 (304 °C) and CoO$_x$-CN-500 (315 °C) [44]. The further reduction of Co(II) to Co(0) appears at higher temperature as observed for CoO$_x$-CN-300 at 359 °C, CoO$_x$-CN-400 at 388 °C and CoO$_x$-CN-500 at 399 °C [45]. The better low-temperature reducibility of catalyst is more favorable to catalytic oxidation activity, which is also verified by the initial hydrogen consumption rate ($r_{initial}$) of CoO$_x$-CN-300 with the maximum value in the low-temperature region (Fig. 5d). The total H_2 uptake amount of the samples (Table 3) was also calculated and CoO$_x$/CN-400 and CoO$_x$/CN-500 show higher consumption than CoO/CN and CoO$_x$/CN-300, due to the higher content of Co_3O_4. Furthermore, the investigation of oxygen storage capacity (OSC) shows the amount of oxygen consumption as follows: CoO$_x$-CN-400 (12.8 μmol/g) > CoO$_x$-CN-300 (12.0 μmol/g) > CoO$_x$-CN-500 (8.0 μmol/g) > CoO-CN (4.8 μmol/g), indicating CoO$_x$-CN-400 and CoO$_x$-CN-300 have the better resupply capacity of oxygen species (Table 1). Summarily, the good photothermocatalytic activity of toluene oxidation over CoO$_x$-CN-300 is the result of synergistic effect of high specific surface area, stronger light absorption, excellent ability of light to heat, appropriate ratios of Co(III)/Co(II) and O_{ads}/O_{latt}, abundant oxygen species and active sites, better mobility of O_{latt} and low-temperature reducibility.

To investigate the source of catalytic activities, photothermocatalysis and thermocatalysis over CoO$_x$-CN-300 supplied by light irradiation and electrical heating for toluene degradation at different temperatures were carried out, respectively. As displayed in Figs. 6a and b, the photothermocatalytic activity is higher than thermocatalytic activity especially in high-temperature region, which directly suggests that light has a great promotion in the catalytic oxidation of toluene. In order to avoid thermal effect, the low-temperature catalytic test over CoO$_x$-CN-300 under UV–vis light by filtering IR region and controlling reactor temperature (39 °C) was implemented, as displayed in Fig. S7, which only displays toluene conversion (50% in 120 min) and no CO_2 formation. It implies that photocatalysis can activate and preliminarily decompose toluene but temperature plays an important role in toluene mineralization [41]. The investigation of photocurrent of all samples (Fig. S8) shows CoO$_x$-CN-300 with the maximum photocurrent density, which is consistent with the catalytic activity trend under full spectrum. Generally, photocurrent is used to evaluate the separation efficiency of photogenerated charge carriers. The distinctly boosted photocurrent
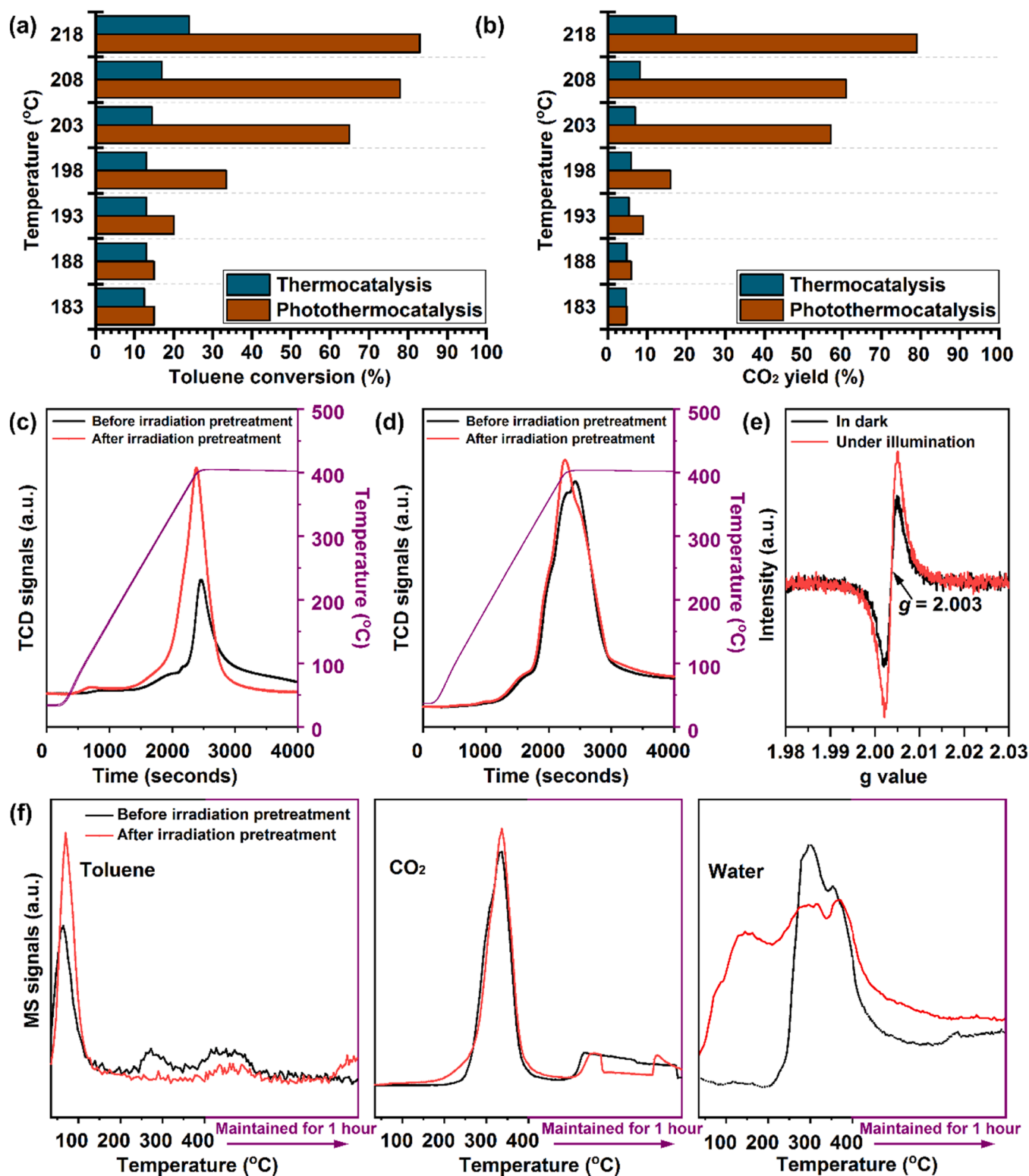
Fig. 6. (a) Toluene conversion and (b) CO_2 yield over CoO_x-CN-300 supplied by light and electrical heating, respectively, (c) O_2-TPD and (d) H_2-TPR profiles over CoO_x-CN-300 before irradiation pretreatment and after irradiation pretreatment, (e) EPR signals over CoO_x-CN-300 obtained at room temperature in dark and under illumination, (f) toluene ($m/z = 91$), CO_2 ($m/z = 44$), water ($m/z = 18$) signals during the process of toluene-TPD over CoO_x-CN-300 before irradiation pretreatment and after irradiation pretreatment.

densities over CoO_x-CN-300 can be attributed to the emerge of more Co (III) and the doping of partially residual C/N heteroatoms. With the increase of calcination temperature, the reduction of doping amount of C/N heteroatoms weakens the photocurrent densities of CoO_x-CN-400 and CoO_x-CN-500. EPR signals over CoO_x-CN-300 under full spectrum

irradiation (Fig. S9) also demonstrate that active hydroxyl and superoxide radicals related to photocatalysis take part in toluene oxidation. Therefore, it can be deduced that light ignites the catalytic reaction and light-to-thermal conversion generates high temperature to complete oxidize intermediates in the photothermocatalytic process.
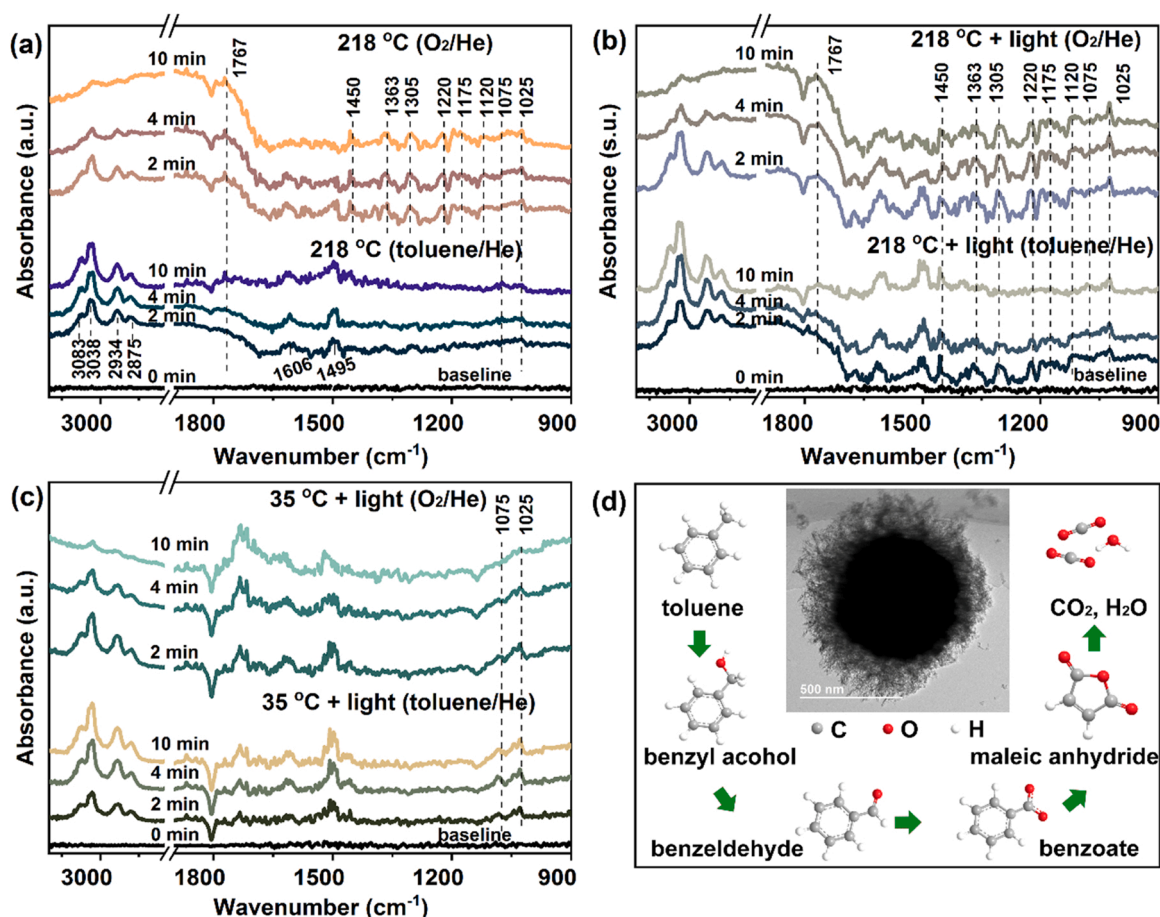
Fig. 7. *In situ* DRIFT spectra over CoO_x-CN-300 for toluene catalytic oxidation under the conditions of (a) electrical heating (218 °C), (b) light irradiation with intensity of 451 mW/cm^2 (218 °C), (c) light irradiation with intensity of 451 mW/cm^2 (35 °C), (d) proposed toluene degradation pathway over CoO_x-CN-300.

An insight into the activation effect of light was further comprehended by studying O_2-TPD and H_2-TPR, EPR and toluene-TPD of CoO_x-CN-300 before and after irradiation pretreatment. As displayed in Fig. 6c of O_2-TPD profile, the desorption signals of physically adsorbed oxygen (< 200 °C) and surface lattice oxygen (200 – 400 °C) are visibly enhanced after irradiation pretreatment, indicating the good activation ability of light to produce more active oxygen species. Similarly, the amount of H_2 consumption after irradiation pretreatment (Fig. 6d) shows the higher value, in particular with high temperature (around 400 °C), which verifies photoactivation enhance the migration of more surface lattice oxygen to react with H_2. In addition, the $r_{initial}$ in the low-temperature region (Fig. S10) is also improved after irradiation pretreatment, contributing to the better catalytic oxidation activity under light irradiation. The enhanced EPR signal under light irradiation at g = 2.003 assigned to the oxygen vacancies indicates that more active lattice oxygen species are released to participate in reaction and provide more active sites to adsorb and activate toluene molecules. It was further confirmed by toluene-TPD experiment over CoO_x-CN-300 before and after irradiation pretreatment (Fig. 6f). Compared to the condition without pretreatment, the desorption signal of toluene and also the signals of CO_2 and water are both intensified via irradiation pretreatment, which explains that light irradiation facilitates the adsorption and activation of toluene and the formation of more active lattice oxygen. Furthermore, even in the absence of gaseous O_2, it still observes the generation of more CO_2 and H_2O whether with irradiation pretreatment or not, which states the Mars-van Krevelen reaction mechanism over CoO_x-CN-300 by reacting surface lattice oxygen with the adsorbed toluene [35].

3.4. *In situ* DRIFTS study

In situ DRIFTS experiments were performed over CoO_x-CN-300 under the conditions of electrical heating and light irradiation, respectively. As exhibited in Fig. 7a, after toluene adsorption for 10 min, it can clearly observe the C-H stretching vibration of the aromatic ring of toluene at 3083 and 3038 cm^{-1}, the skeleton vibration of aromatic ring at 1606 and 1495 cm^{-1}, and the C-H symmetric and asymmetric stretching of methylene group at 2934 and 2875 cm^{-1} [46]. Meanwhile, the new peaks appeared at 1075 and 1025 cm^{-1} are ascribed to C-O stretching vibration of benzyl alcohol, suggesting the activation of toluene by surface lattice oxygen [47]. When external O_2 is introduced after toluene adsorption, and more kinds of intermediates are formed and the aromatic ring is gradually destroyed. The peaks at 1450, 1305 and 1175 cm^{-1} are indexed to the C=C bond of the aromatic skeleton and the C=O bond of benzaldehyde. The peaks at 1767 and 1363 cm^{-1} are associated with the C=O and C-O stretching vibration of benzoic acid. The peaks at 1120 and 1075 cm^{-1} correspond to the vibrational peaks of maleic anhydride. In contrast to pure thermocatalysis, at the same conditions, the existence of light not only increases toluene adsorption on the surface but also immediately convert some adsorbed toluene into intermediates even to be complete oxidized by more photoactivated lattice oxygen (Fig. 7b). The introduction of oxygen results in reemergence of more intermediates on the surface, which is due to light irradiation and activation of gaseous O_2 to form more surface lattice oxygen involved in catalytic oxidation of toluene. The low-temperature irradiation experiment at 35 °C (Fig. 7c) also observe the formation of benzyl alcohol in the initial stage of toluene adsorption, but there are no deep-oxidized intermediates such as benzaldehyde and benzoic acid
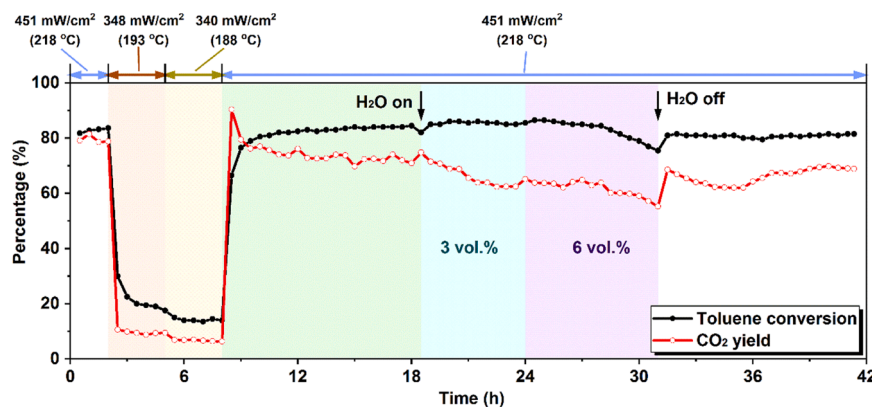
Fig. 8. Catalytic stability over CoO_x-CN-300 under irradiation of different light intensities with different contents of water vapor.

produced even in the presence of O_2, proving that reaction temperature is vital for complete catalytic oxidation of toluene. In brief, photo-thermocatalytic oxidation of toluene over CoO_x-CN-300 is actually light-driven thermocatalytic process accompanying with photocatalytic behavior and it follows the Mars-van Krevelen (MvK) mechanism. According to the analysis of in situ DRIFTS and on-line mass spectrum (Fig. S11), the degradation pathway of toluene on CoO_x-CN-300 obeys the route of toluene → benzyl alcohol → benzaldehyde → benzoate → maleic anhydride → CO_2, H_2O (Fig. 7d).

3.5. Stability tests of CoO_x-CN-300

Continuous photothermocatalytic performance of toluene oxidation over CoO_x-CN-300 was conducted, as displayed in Fig. 8. With high light intensity of 451 mW/cm^2 (catalyst temperature at 218 °C), it can stably maintain toluene conversion and mineralization of around 80% for 2 h. When light intensities are reduced to 348 mW/cm^2 (193 °C) and 340 mW/cm^2 (188 °C), both toluene conversion and mineralization decrease to less than 20% with the better stability for at least 6 h. Further elevation to 451 mW/cm^2 with the temperature of 218 °C, the catalyst can still achieve 84% conversion and 72% CO_2 yield at least for 10 h. The slight drop of CO_2 yield may be due to the occupation of surface-active sites by carbonaceous intermediates. Introducing 3 vol% water vapor, toluene conversion can keep in 6 h but mineralization continues to decrease to 62.5%. When the water content is increased to 6 vol%, it leads to the obvious decline of toluene conversion and CO_2 yield to 75% and 57% within 8 h, respectively. It is mainly attributed to the competitive adsorption of toluene and water on the surface of catalyst. Besides, as to the results of in situ DRIFTS experiments (Fig. 7), it is found that toluene is activated on the lattice oxygen of CoO_x-CN-300 and oxidized to benzyl alcohol in the absence of oxygen. Further introduction of oxygen promotes deep oxidation. There is also competitive adsorption between intermediate products and water on active sites. From the perspective of reaction equilibrium, the introduction of water vapor reduces the partial pressure of reactant oxygen and water vapor as a product is also not conducive to the oxidation of toluene. Therefore, the introduction of water vapor has a greater impact on CO_2 mineralization than on toluene conversion. However, it can recover to the approximate original level quickly after cutting off water vapor and retains the photothermocatalytic stability for at least 10 h. Therefore, it can infer that CoO_x-CN-300 owns the desirable catalytic performance, long-term stability and good water durability in the photothermocatalysis.

4. Conclusion

In conclusion, a CN-induced urchin-like catalyst CoO_x-CN surrounded by rich branches was synthesized by the solvothermal and calcination method at different temperatures. At an appropriate calcination temperature (300 °C), partial CN structure was destroyed and removed from the bulk, thus modifying the electronic structure of CoO_x. By comparison, CoO_x-CN-300, which possessed large specific surface area, superior light absorption capacity, good oxygen desorption and migration ability and enough active sites (Co(III) and oxygen vacancies), exhibited the good catalytic activity with toluene conversion of 83.8% and CO_2 yield of 79.6% under the full spectrum irradiation. Furthermore, it has been proved that light irradiation significantly promotes the light-driven thermocatalytic performance compared to conventional thermocatalytic activity by activating more lattice oxygen and inducing the generation of more oxygen vacancies to participate in the oxidation reaction. This work proposes a feasible method to regulate the role of photocatalysis and thermocatalysis in the photothermocatalytic process through C/N heteroatom doping, which is helpful to understand the process of photothermocatalysis of VOCs.

CRediT authorship contribution statement

Meng Zhang: Conceptualization, Methodology, Investigation, Resources, Writing – original draft. **Hui Gao:** Methodology, Investigation, Resources. **Jing Chen:** Writing – review & editing. **Ehiaghe Agbovhimen Elimian:** Methodology. **Hongpeng Jia:** Supervision, Writing – review & editing, Project administration, Funding acquisition.

Declaration of Competing Interest

The authors declare that they have no known competing financial interests or personal relationships that could have appeared to influence the work reported in this paper.

Notes

The authors declare no competing financial interest.

Appendix A. Supporting information

Supplementary data associated with this article can be found in the online version at doi:10.1016/j.apcatb.2022.121208.

References

[1] X. Liang, X. Chen, J. Zhang, T. Shi, X. Sun, L. Fan, L. Wang, D. Ye, Reactivity-based industrial volatile organic compounds emission inventory and its implications for ozone control strategies in China, Atmos. Environ. 162 (2017) 115–126, https://doi.org/10.1016/j.atmosenv.2017.04.036.

[2] C. He, J. Cheng, X. Zhang, M. Douthwaite, S. Pattisson, Z. Hao, Recent advances in the catalytic oxidation of volatile organic compounds: a review based on pollutant sorts and sources, Chem. Rev. 119 (2019) 4471–4568, https://doi.org/10.1021/acs.chemrev.8b00408.

[3] J. Li, M. Zhang, E.A. Elimian, X. Lv, J. Chen, H. Jia, Convergent ambient sunlight-powered multifunctional catalysis for toluene abatement over in situ exsolution of Mn₃O₄ on perovskite parent, Chem. Eng. J. 412 (2021), https://doi.org/10.1016/j.cej.2021.128560.

[4] A.H. Mamaghani, F. Haghighat, C.S. Lee, Photocatalytic oxidation technology for indoor environment air purification: the state-of-the-art, Appl. Catal. B 203 (2017) 247–269, https://doi.org/10.1016/j.apcatb.2016.10.037.

[5] F. Liu, M. Zeng, Y. Li, Y. Yang, M. Mao, X. Zhao, UV–vis–infrared light driven thermocatalytic activity of octahedral layered birnessite nanoflowers enhanced by a novel photoactivation, Adv. Funct. Mater. 26 (2016) 4518–4526, https://doi.org/10.1002/adfm.201601046.

[6] L. Lan, Z. Shi, Q. Zhang, Y. Li, Y. Yang, S. Wu, X. Zhao, Defects lead to a massive enhancement in the UV-Vis-IR driven thermocatalytic activity of Co₃O₄ mesoporous nanorods, J. Mater. Chem. A 6 (2018) 7194–7205, https://doi.org/10.1039/C8TA01362D.

[7] J. Chen, D. Yan, Z. Xu, X. Chen, X. Chen, W. Xu, H. Jia, J. Chen, A. Novel, Redox precipitation to synthesize Au-doped α-MnO₂ with high dispersion toward low-temperature oxidation of formaldehyde, Environ. Sci. Technol. 52 (2018) 4728–4737, https://doi.org/10.1021/acs.est.7b06039.

[8] Y. Shen, J. Deng, S. Impeng, S. Li, T. Yan, J. Zhang, L. Shi, D. Zhang, Boosting toluene combustion by engineering Co–O strength in cobalt oxide catalysts, Environ. Sci. Technol. 54 (2020) 10342–10350, https://doi.org/10.1021/acs.est.0c02680.

[9] L. Zhuang, L. Ge, Y. Yang, M. Li, Y. Jia, X. Yao, Z. Zhu, Ultrathin iron-cobalt oxide nanosheets with abundant oxygen vacancies for the oxygen evolution reaction, Adv. Mater. 29 (2017), 1606793, https://doi.org/10.1002/adma.201606793.

[10] X. Wang, Y. Liu, T. Zhang, Y. Luo, Z. Lan, K. Zhang, J. Zuo, L. Jiang, R. Wang, Geometrical-site-dependent catalytic activity of ordered mesoporous Co-based spinel for benzene oxidation: in situ DRIFTS study coupled with Raman and XAFS spectroscopy, ACS Catal. 7 (2017) 1626–1636, https://doi.org/10.1021/acscatal.6b03547.

[11] X. Yang, X. Yu, M. Jing, W. Song, J. Liu, M. Ge, Defective MnₓZr₁₋ₓO₂ solid solution for the catalytic oxidation of toluene: insights into the oxygen vacancy contribution, ACS Appl. Mater. Interfaces 11 (2019) 730–739, https://doi.org/10.1021/acsami.8b17062.

[12] X. Chen, J. Li, S. Cai, J. Chen, H. Jia, Two-step pyrolytic engineering of carbon-doped Co₃O₄ with rich defects for efficient low-temperature CO oxidation, J. Mater. Chem. A 8 (2020) 6619–6630, https://doi.org/10.1039/c9ta13488c.

[13] M. Lykaki, E. Pachatouridou, S.A.C. Carabineiro, E. Iliopoulou, C. Andriopoulou, N. Kallithrakas-Kontos, S. Boghosian, M. Konsolakis, Ceria nanoparticles shape effects on the structural defects and surface chemistry: implications in CO oxidation by Cu/CeO₂ catalysts, Appl. Catal. B 230 (2018) 18–28, https://doi.org/10.1016/j.apcatb.2018.02.035.

[14] S. Li, L. Zhang, S. Jie, Z. Liu, In situ synthesis of highly dispersed Co–N–C catalysts with carbon-coated sandwich structures based on defect anchoring, New J. Chem. 44 (2020) 5404–5409, https://doi.org/10.1039/D0NJ00213E.

[15] G. Zhang, C. Huang, X. Wang, Dispersing molecular cobalt in graphitic carbon nitride frameworks for photocatalytic water oxidation, Small 11 (2015) 1215–1221, https://doi.org/10.1002/smll.201402636.

[16] M. Zhang, S. Cai, J. Li, E.A. Elimian, J. Chen, H. Jia, Ternary multifunctional catalysts of polymeric carbon nitride coupled with Pt-embedded transition metal oxide to enhance light-driven photothermal catalytic degradation of VOCs, J. Hazard. Mater. 412 (2021), 125266, https://doi.org/10.1016/j.jhazmat.2021.125266.

[17] H. Zhou, T. Liu, X. Zhao, Y. Zhao, H. Lv, S. Fang, X. Wang, F. Zhou, Q. Xu, J. Xu, C. Xiong, Z. Xue, K. Wang, W.-C. Cheong, W. Xi, L. Gu, T. Yao, S. Wei, X. Hong, J. Luo, Y. Li, Y. Wu, A supported nickel catalyst stabilized by a surface digging effect for efficient methane oxidation, Angew. Chem. Int. Ed. 58 (2019) 18388–18393, https://doi.org/10.1002/anie.201912785.

[18] J. Wang, X. Duan, J. Gao, Y. Shen, X. Feng, Z. Yu, X. Tan, S. Liu, S. Wang, Roles of structure defect, oxygen groups and heteroatom doping on carbon in nonradical oxidation of water contaminants, Water Res. 185 (2020), 116244, https://doi.org/10.1016/j.watres.2020.116244.

[19] Y. Wang, X. Duan, Y. Xie, H. Sun, S. Wang, Nanocarbon-based catalytic ozonation for aqueous oxidation: engineering defects for active sites and tunable reaction pathways, ACS Catal. 10 (2020) 13383–13414, https://doi.org/10.1021/acscatal.0c04232.

[20] Z. Yang, X. Duan, J. Wang, Y. Li, X. Fan, F. Zhang, G. Zhang, W. Peng, Facile synthesis of high-performance nitrogen-doped hierarchically porous carbon for catalytic oxidation, ACS Sustain. Chem. Eng. 8 (2020) 4236–4243, https://doi.org/10.1021/acssuschemeng.9b07469.

[21] H. Yang, J. Ouyang, A. Tang, Single step synthesis of high-purity CoO nanocrystals, J. Phys. Chem. B 111 (2007) 8006–8013, https://doi.org/10.1021/jp070711k.

[22] Y. He, L. Zhang, B. Teng, M. Fan, New application of Z-scheme Ag₃PO₄/g-C₃N₄ composite in converting CO₂ to fuel, Environ. Sci. Technol. 49 (2015) 649–656, https://doi.org/10.1021/es5046309.

[23] D. Adekoya, H. Chen, H.Y. Hoh, T. Gould, M.S.J.T. Balogun, C. Lai, H. Zhao, S. Zhang, Hierarchical Co₃O₄@N-doped carbon composite as an advanced anode material for ultrastable potassium storage, ACS Nano 14 (2020) 5027–5035, https://doi.org/10.1021/acsnano.0c01395.

[24] L. Li, X. Sun, X. Qiu, J. Xu, G. Li, Nature of catalytic activities of CoO nanocrystals in thermal decomposition of ammonium perchlorate, Inorg. Chem. 47 (2008) 8839–8846, https://doi.org/10.1021/ic8008283.

[25] S. Mo, S. Li, J. Li, Y. Deng, S. Peng, J. Chen, Y. Chen, Rich surface Co(iii) ions-enhanced Co nanocatalyst benzene/toluene oxidation performance derived from CoIICoIII layered double hydroxide, Nanoscale 8 (2016) 15763–15773, https://doi.org/10.1039/C6NR04902H.

[26] X. Chen, J.-J. Li, X. Chen, S.-C. Cai, E.-Q. Yu, J. Chen, H. Jia, MOF-templated approach for hollow NiOx/Co₃O₄ catalysts: enhanced light-driven thermocatalytic degradation of toluene, ACS Appl. Nano Mater. 1 (2018) 2971–2981, https://doi.org/10.1021/acsanm.8b00587.

[27] K. Xiang, Z. Xu, T. Qu, Z. Tian, Y. Zhang, Y. Wang, M. Xie, X. Guo, W. Ding, X. Guo, Two dimensional oxygen-vacancy-rich Co₃O₄ nanosheets with excellent supercapacitor performances, Chem. Commun. 53 (2017) 12410–12413, https://doi.org/10.1039/C7CC07515D.

[28] F. Guo, W. Shi, C. Zhu, H. Li, Z. Kang, CoO and g-C₃N₄ complement each other for highly efficient overall water splitting under visible light, Appl. Catal. B 226 (2018) 412–420, https://doi.org/10.1016/j.apcatb.2017.12.064.

[29] O. Brummel, Y. Lykhach, M. Vorokhta, B. Šmíd, C. Stumm, F. Faisal, T. Skála, N. Tsud, A. Neitzel, K. Beranová, K.C. Prince, V. Matolín, J. Libuda, Redox behavior of Pt/Co₃O₄(111) model electrocatalyst studied by X-ray photoelectron spectroscopy coupled with an electrochemical cell, J. Phys. Chem. C 123 (2019) 8746–8758, https://doi.org/10.1021/acs.jpcc.8b08890.

[30] D. Cabrera-German, G. Gomez-Sosa, A. Herrera-Gomez, Accurate peak fitting and subsequent quantitative composition analysis of the spectrum of Co 2p obtained with Al Kα radiation: I: cobalt spinel, Surf. Interface Anal. 48 (2016) 252–256, https://doi.org/10.1002/sia.5933.

[31] Y. Cai, J. Xu, Y. Guo, J. Liu, Ultrathin, polycrystalline, two-dimensional Co₃O₄ for low-temperature CO oxidation, ACS Catal. 9 (2019) 2558–2567, https://doi.org/10.1021/acscatal.8b04064.

[32] Z. Sun, T. Liao, Y. Dou, S.M. Hwang, M.-S. Park, L. Jiang, J.H. Kim, S.X. Dou, Generalized self-assembly of scalable two-dimensional transition metal oxide nanosheets, Nat. Commun. 5 (2014) 3813, https://doi.org/10.1038/ncomms4813.

[33] D. Kochubey, V. Kaichev, A. Saraev, S. Tomyn, A. Belov, Y. Voloshin, Combined X-ray absorption near-edge structure and X-ray photoelectron study of the electrocatalytically active cobalt(I) cage complexes and the clathrochelate cobalt (II)- and cobalt(III)-containing precursors and analogs, J. Phys. Chem. C 117 (2013) 2753–2759, https://doi.org/10.1021/jp3085606.

[34] W. Liu, R. Liu, H. Zhang, Q. Jin, Z. Song, X. Zhang, Fabrication of Co₃O₄ nanospheres and their catalytic performances for toluene oxidation: the distinct effects of morphology and oxygen species, Appl. Catal. A Gen. 597 (2020), 117539, https://doi.org/10.1016/j.apcata.2020.117539.

[35] Q. Zhao, Y. Zheng, C. Song, Q. Liu, N. Ji, D. Ma, X. Lu, Novel monolithic catalysts derived from in-situ decoration of Co₃O₄ and hierarchical Co₃O₄@MnOₓ on Ni foam for VOC oxidation, Appl. Catal. B 265 (2020), 118552, https://doi.org/10.1016/j.apcatb.2019.118552.

[36] J. Zhong, Y. Zeng, D. Chen, S. Mo, M. Zhang, M. Fu, J. Wu, Z. Su, P. Chen, D. Ye, Toluene oxidation over Co³⁺-rich spinel Co₃O₄: evaluation of chemical and by-product species identified by in situ DRIFTS combined with PTR-TOF-MS, J. Hazard. Mater. 386 (2020), 121957, https://doi.org/10.1016/j.jhazmat.2019.121957.

[37] J. Hong, J. Du, B. Wang, Y. Zhang, C. Liu, H. Xiong, F. Sun, S. Chen, J. Li, Plasma-assisted preparation of highly dispersed cobalt catalysts for enhanced Fischer–Tropsch synthesis performance, ACS Catal. 8 (2018) 6177–6185, https://doi.org/10.1021/acscatal.8b00960.

[38] L. Wang, X. Xu, S. Wu, F. Cao, Nonstoichiometric tungsten oxide residing in a 3D nitrogen doped carbon matrix, a composite photocatalyst for oxygen vacancy induced VOC degradation and H2 production, Catal. Sci. Technol. 8 (2018) 1366–1374, https://doi.org/10.1039/C7CY02572F.

[39] Y. Cui, X. Ding, X. Fu, X. Wang, Construction of conjugated carbon nitride nanoarchitectures in solution at low temperatures for photoredox catalysis, Angew. Chem. Int. Ed. 51 (2012) 11814–11818, https://doi.org/10.1002/anie.201206534.

[40] D. Luo, S. Liu, J. Liu, J. Zhao, C. Miao, J. Ren, Catalytic combustion of toluene over cobalt oxides supported on graphitic carbon nitride (CoOₓ/g-C₃N₄) catalyst, Ind. Eng. Chem. Res. 57 (2018) 11920–11928, https://doi.org/10.1021/acs.iecr.8b02625.

[41] E. Yu, J. Chen, H. Jia, Enhanced light-driven photothermocatalytic activity on selectively dissolved LaTi₁₋ₓMnₓO₃₊delta perovskites by photoactivation, J. Hazard. Mater. 399 (2020), 122942, https://doi.org/10.1016/j.jhazmat.2020.122942.

[42] X. Chen, Q. Li, M. Zhang, J. Li, S. Cai, J. Chen, H. Jia, MOF-templated preparation of highly dispersed Co/Al₂O₃ composite as the photothermal Catalyst with high solar-to-fuel efficiency for CO₂ methanation, ACS Appl. Mater. Interfaces 12 (2020) 39304–39317, https://doi.org/10.1021/acsami.0c11576.

[43] Y. He, X. Liu, G. Chen, J. Pan, A. Yan, A. Li, X. Lu, D. Tang, N. Zhang, T. Qiu, R. Ma, T. Sasaki, Synthesis of Co(II)-Fe(III) hydroxide nanocones with mixed octahedral/tetrahedral coordination toward efficient electrocatalysis, Chem. Mater. 32 (2020) 4232–4240, https://doi.org/10.1021/acs.chemmater.0c00512.

[44] F. Hu, Y. Peng, J. Chen, S. Liu, H. Song, J. Li, Low content of CoOₓ supported on nanocrystalline CeO₂ for toluene combustion: the importance of interfaces between active sites and supports, Appl. Catal. B 240 (2019) 329–336, https://doi.org/10.1016/j.apcatb.2018.06.024.

[45] J. Ding, L. Li, H. Zheng, Y. Zuo, X. Wang, H. Li, S. Chen, D. Zhang, X. Xu, G. Li, Co_3O_4–$CuCoO_2$ nanomesh: an interface-enhanced substrate that simultaneously promotes CO adsorption and O_2 activation in H_2 purification, ACS Appl. Mater. Interfaces 11 (2019) 6042–6053, https://doi.org/10.1021/acsami.8b19478.

[46] J.-J. Li, E.-Q. Yu, S.-C. Cai, X. Chen, J. Chen, H.-P. Jia, Y.-J. Xu, Noble metal free, CeO2/LaMnO3 hybrid achieving efficient photo-thermal catalytic decomposition

of volatile organic compounds under IR light, Appl. Catal. B 240 (2019) 141–152, https://doi.org/10.1016/j.apcatb.2018.08.069.

[47] Y. Shen, J. Deng, S. Impeng, S. Li, T. Yan, J. Zhang, L. Shi, D. Zhang, Boosting toluene combustion by engineering Co-O strength in cobalt oxide catalysts, Environ. Sci. Technol. 54 (2020) 10342–10350, https://doi.org/10.1021/acs.est.0c02680.